Determination of the Internal Morphology of Nanostructures Patterned by Directed Self Assembly

Daniel F. Sunday,[†] Matthew R. Hammond,[†] Chengqing Wang,[†] Wen-li Wu,[†] Dean M. Delongchamp,[†] Melia Tjio,[‡] Joy Y. Cheng,[‡] Jed W. Pitera,[‡] and R. Joseph Kline[†,*]

[†]Materials Science and Engineering Division, National Institute of Standards and Technology, Gaithersburg, Maryland 20899, United States and [‡]IBM Research — Almaden, San Jose, California 95120, United States

ABSTRACT

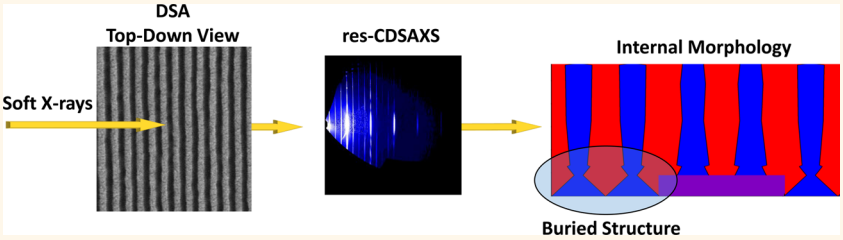

The directed self-assembly (DSA) of block copolymers (BCP) is an emerging resolution enhancement tool that can multiply or subdivide the pitch of a lithographically defined chemical or topological pattern and is a resolution enhancement candidate to augment conventional lithography for patterning sub-20 nm features. Continuing the development of this technology will require an improved understanding of the polymer physics involved as well as experimental confirmation of the simulations used to guide the design process. Both of these endeavors would be greatly facilitated by a metrology, which is capable of probing the internal morphology of a DSA film. We have developed a new measurement technique, resonant critical-dimension small-angle X-ray scattering (res-CDSAXS), to evaluate the 3D buried features inside the film. This is an X-ray scattering measurement where the sample angle is varied to probe the 3D structure of the film, while resonant soft X-rays are used to enhance the scattering contrast. By measuring the same sample with both res-CDSAXS and traditional CDSAXS (with hard X-rays), we are able to demonstrate the dramatic improvement in scattering obtained through the use of resonant soft X-rays. Analysis of the reciprocal space map constructed from the res-CDSAXS measurements allowed us to reconstruct the complex buried features in DSA BCP films. We studied a series of DSA BCP films with varying template widths, and the internal morphologies for these samples were compared to the results of single chain in mean-field simulations. The measurements revealed a range of morphologies that occur with changing template width, including results that suggest the presence of mixed morphologies composed of both whole and necking lamella. The development of res-CDSAXS will enable a better understanding of the fundamental physics behind the formation of buried features in DSA BCP films.

KEYWORDS: directed self assembly · block copolymer · soft X-ray · resonant scattering

Advances in lithographic patterning techniques have driven the densification of features on integrated circuits since the birth of the modern semiconductor industry. 193 nm immersion lithography is the current industry standard, but fundamental limits are now being reached that prevent the technology from being capable of patterning the feature sizes required for next generation technology nodes.[1] Creative solutions such as multiple patterning schemes have extended this technique down to a half-pitch of 22 nm or below at the expense of longer processing times and significantly increased fabrication costs. This approach may be stretched to quadruple patterning and beyond, but there is an economic incentive to find alternatives that reduce patterning cost and provide high patterning quality such as good critical dimension uniformity and line edge/width roughness (LER/LWR).[1] A myriad of candidate technologies have been proposed to enable the necessary reduction in critical dimension (CD), including a shift to extreme ultraviolet (EUV) sources,[2] nanoimprint lithography,[3] direct write electron-beam patterning[4] and implementing hybrid

* Address correspondence to rjkline@nist.gov.

Received for review May 29, 2014 and accepted July 30, 2014.

Published online July 30, 2014
10.1021/nn5029289

techniques such as pattern amplification through the directed self-assembly (DSA) of block copolymers (BCP).[5−9] BCP's are well-known to self-assemble into an array of morphologies (spheres, cylinders and lamella among others) as a function of the volume fractions of the component blocks.[10] DSA takes advantage of this property by using a chemical or topographic template to guide the uniform, long-range orientation of the BCP. Compositional differences between the blocks enable conversion of the patterned film into an etch mask, which can transfer the pattern into the underlying layers. This approach has moved from laboratories to pilot lines over past few years. The primary challenge remaining before DSA can attain widespread use in the semiconductor industry is the presence of defects.[11] This includes both registration defects, where the polymer does not align properly with the guiding pattern, and internal morphological defects, which can disrupt pattern transfer to the underlying wafer. Concerns that these defects may derail the implementation of DSA into the production environment have driven a considerable modeling effort focused on understanding the mechanisms and driving forces behind defect formation.[9,12−22] These simulations provide useful insights into the self-assembly process, but at present cannot be directly connected to processing parameters. Unfortunately none of the metrologies typically used to characterize thin films are capable of interrogating the three-dimensional structure of buried features in sub-30 nm pitch DSA BCP films. We report on the development of a new technique capable of reconstructing the complex lamellar profiles of industrially relevant frequency multiplication DSA films. This new measurement is a variation on critical-dimension small-angle X-ray scattering (CDSAXS), a transmission X-ray scattering measurement identified by the International Technology Roadmap for Semiconductors (ITRS) as a potential next generation 3D dimensional metrology tool for periodic nanostructures.[1,23−25] We have combined CDSAXS with soft X-rays to obtain resonant contrast between the BCP components, resulting in a measurement method (res-CDSAXS) capable of interrogating the buried 3D structures in a DSA BCP film.

Figure 1A shows the outline of the DSA process using chemoepitaxy, where a chemical template is patterned in a very thin (<10 nm) layer of polymer using conventional lithographic techniques (e-beam,[9,26] EUV[27,28] and 193 nm immersion lithography[29] have all been used in template patterning). The samples in this study were patterned using 193 nm immersion lithography through a liftoff approach, which results in both chemical and topological heterogeneity in the template.[29] Once the template has been patterned a thin film of BCP is deposited and annealed above its glass transition temperature, enabling the BCP to register with the template pattern. This process is driven by the minimization of interfacial energy at the surface and substrate.[30,31] Long range registration occurs when the BCP pitch is commensurate with the template pitch, with most reports demonstrating 2× or 4× density multiplication.[29] This ability to amplify the underlying pattern is the real value to the technique as it allows for the production of features with CDs below what other high volume lithographic techniques are currently capable of. Polystyrene-*b*-poly(methyl methacrylate) (PS-*b*-PMMA) is the BCP most commonly used in this process, but more recent studies have investigated the use of alternative BCP's which either exhibit larger Flory−Huggins interaction parameters (χ), promoting smaller pitches and interfacial widths, or improved native etch contrast (in some cases both).[32−34] The recent integration of DSA into a 300 mm wafer track demonstrates the feasibility of scaling up the process into a manufacturing environment, a major milestone on the road to the widespread adoption of the technology.[35]

X-ray scattering techniques such as SAXS and grazing incidence SAXS (GISAXS) are common characterization tools for BCP films. Unfortunately neither technique is ideally suited to interrogate the internal morphology of DSA films, SAXS is typically performed on much thicker, randomly oriented films and lacks the sensitivity to the detailed profile of the lamellae. GISAXS is capable of interrogating sub-100 nm films and has been used to determine the morphology and order of thin film BCP's, but determining the detailed structure of line gratings is difficult due to the need to use dynamic diffraction theory in the profile reconstruction.[37,38] These GISAXS modeling approaches have been used to determine the scattering pattern for a given nanostructure, but become intractable for the large number of iterations necessary for the inverse fitting routines used to solve for complex shapes and also will have difficulties with finding a unique inverse solution. CDSAXS was developed as an adaptation to traditional SAXS in order to characterize the 2D or 3D shape of periodic nanostructures in thin films. CDSAXS (Figure 1B) is a variable-angle, transmission scattering measurement where a series of diffraction patterns at different incident angles are used to reconstruct the 2D or 3D reciprocal space map from a periodic nanostructure. The shape of the measured nanostructure is determined by fitting the reciprocal space map using an inverse, iterative approach.[23,39,40] This method has been shown to be effective at characterizing both very simple line gratings and also more complex structures such as finFETs, which contain multiple sidewall angles and materials.[41] The challenge for X-ray methods with thin organic films is that the contrast between the components is minimal, and as a result the scattered intensity is insufficient for reconstructing complex nanoscale features. Historically, controlling contrast between layers in block copolymers requires one of

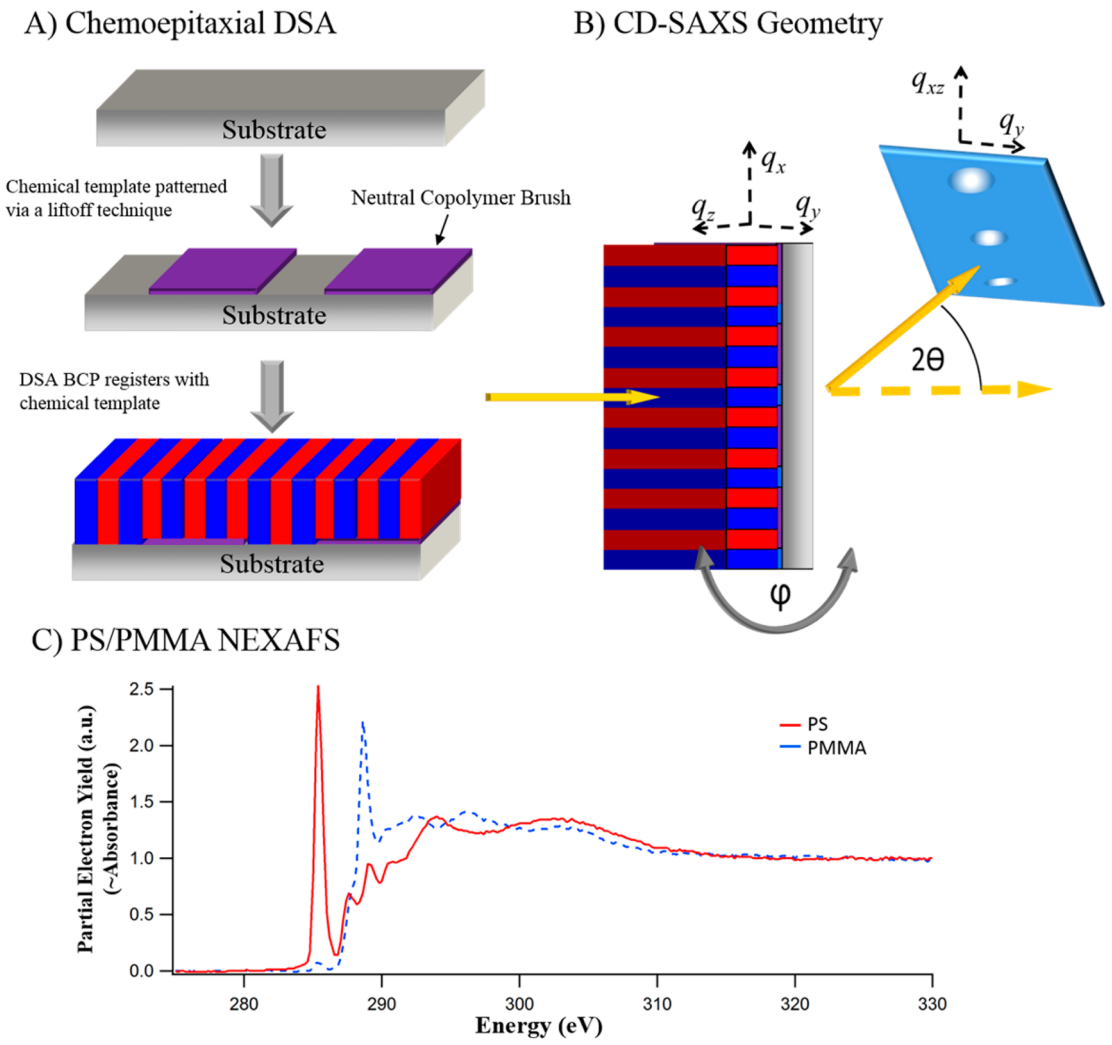

Figure 1. (A) Outline of the DSA process, where the chemical template is patterned *via* a liftoff technique and a lamellar BCP is self-assembled on top of the template at 4× density multiplication. (B) CDSAXS geometry including definition of the *q* vectors at the sample and detector. (C) NEXAFS spectrum of PS (solid red line) and PMMA (dashed blue line), illustrating the sharp absorbance peak for PS at ≈285 eV and PMMA at ≈289 eV. Detailed values for the refractive index of PS and PMMA are available in the literature.[36]

the blocks be either doped with a heavy metal for transmission electron microscopy (TEM) measurements or deuterated for neutron scattering, but both approaches risk altering the original microstructure.[42] Resonant soft X-rays provide an alternative that can enhance the contrast while allowing the native film to be measured. The complex index of refraction varies sharply near an atomic absorption edge, where a ground state electron is resonantly transferred into an antibonding state *via* photoabsorption. The incident wavelength which causes this transition depends upon the exact nature of the chemical bonds present in a molecule, for example the excitation of electrons in aromatic and carbonyl carbons will take place at different energies. As a result the scattering contrast between two materials becomes moiety specific around the absorption edge, a property which can be used to dramatically enhance scattering between materials with only small differences in composition, such as organic block copolymers. The near edge X-ray absorption fine structure (NEXAFS) spectra of PS and PMMA shown in Figure 1C provides a clear example of how the chemical structure impacts the exact location of the photoabsorption. The sharp carbon absorption for PS at 285 eV is from the π^* orbitals of the carbon−carbon double bond, while the feature at 289 eV for PMMA is due to the π^* orbital of the carbon−oxygen bond. This difference in the absorption and the associated dielectric constant dispersion gives rise to the scattering contrast between the two materials. The resonant behavior extends several eV away from the maximum of the absorption edge, making it possible to utilize energies below the edge in order to take advantage of the improved contrast from the resonant scattering while minimizing radiation damage to the sample. Resonant soft X-rays have been shown to be effective at characterizing multilayer organic thin films, the evaluation of triblock copolymer

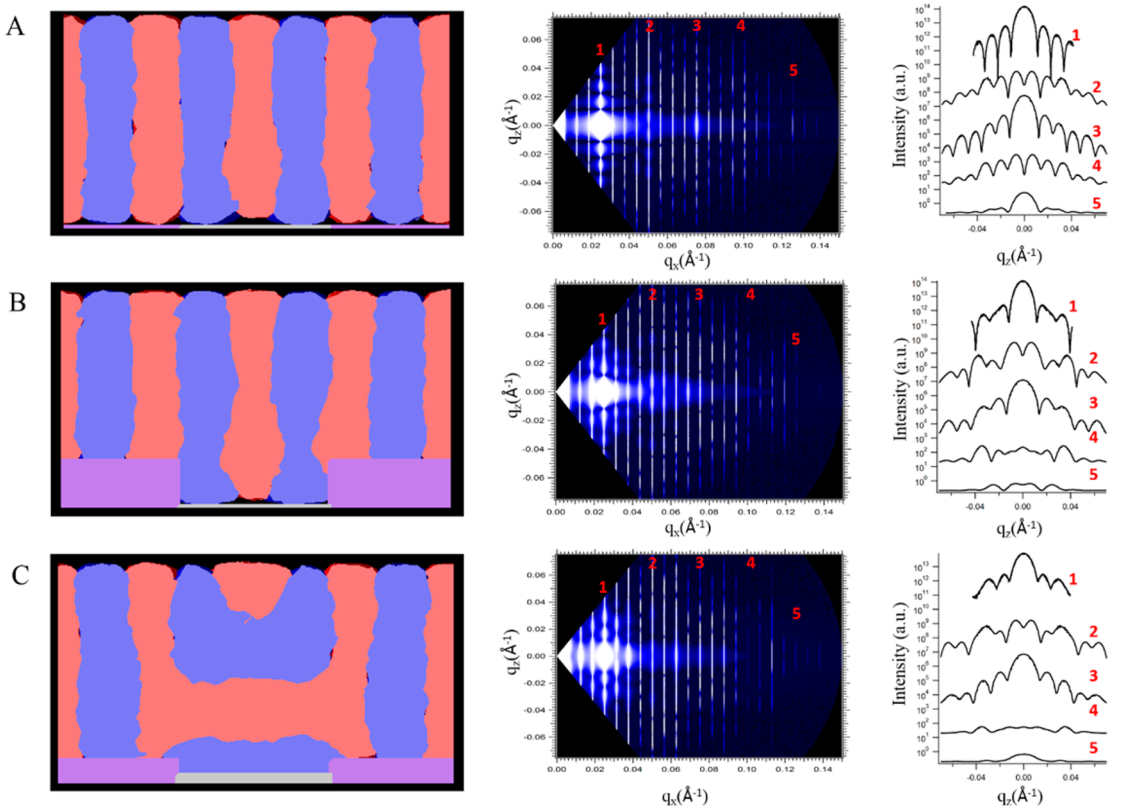

Figure 2. MC results on DSA BCP displaying representative morphologies along with the corresponding simulated res-CDSAXS reciprocal space map and q_z cuts for the primary peak orders (red numerals indicate the primary peak order). All samples were 64 nm tall, with a pinning stripe width equal to 1.5 times the BCP pitch. Blue represents PMMA and red represents PS; the NRCP is shown in purple and the pinning stripe on the substrate in gray. (A) 1:1 pinning stripe:NRCP thickness, (B) 1:14 pinning stripe:NRCP thickness, (C) 3:7 pinning stripe:NRCP thickness, where the increased pinning stripe height effectively represents a more attractive surface for the PMMA block.

morphologies and nanoparticle structure determination.[36,40,43−46] Resonant soft X-rays have also been used to obtain magnetic dipole contrast at the L-edges of common magnetic materials,[47,48] making res-CDSAXS potentially applicable to the magnetic dipole orientation within periodic nanostructured magnetic devices such as spin valve transistors or magnetic memory.

We demonstrate that res-CDSAXS is capable of evaluating the internal structure in a DSA BCP by examining a series of samples where the width of the guiding pattern on the template was varied to induce changes in the buried morphology. Single chain in mean field Monte Carlo (MC) simulations will be used to provide insight into the impact of the template on the internal BCP morphology, and to illustrate the types of buried structures which can manifest within the film. Through analysis of reciprocal space maps generated by both hard X-ray CDSAXS and res-CDSAXS we will demonstrate that the high energy measurements are incapable of reconstructing the buried features inside a typical DSA film, while the resonant scattering generates sufficient information to obtain nanoscale resolution on the sample. To better illustrate this we will examine the differences in the internal film structure induced by the small changes to the chemical template.

RESULTS AND DISCUSSION

Single chain in mean field MC simulations were performed to explore how variations in key process parameters impact the equilibrium morphology, representative results from those simulations are presented in Figure 2. For all three examples shown here the film thickness and chemical template widths were held constant, while the brush thickness and effective affinity of the substrate for the BCP components were varied. Figure 2A shows PS-*b*-PMMA assembled on a chemical template where the ratio of substrate to template thickness was 1:1. In this case the MC calculations predict the formation of vertical lamella with only minor disruptions from their equilibrium structure. The width of the on-substrate PMMA lamella expand slightly at the base (where the PMMA block has a higher affinity for the substrate) and then narrow further up the profile, while the on-brush lamella show only random width variations. Similar results are obtained when the NRCP brush is thicker, as shown in Figure 2B. The expansion and contraction of the on-substrate PMMA lamella are exacerbated by the

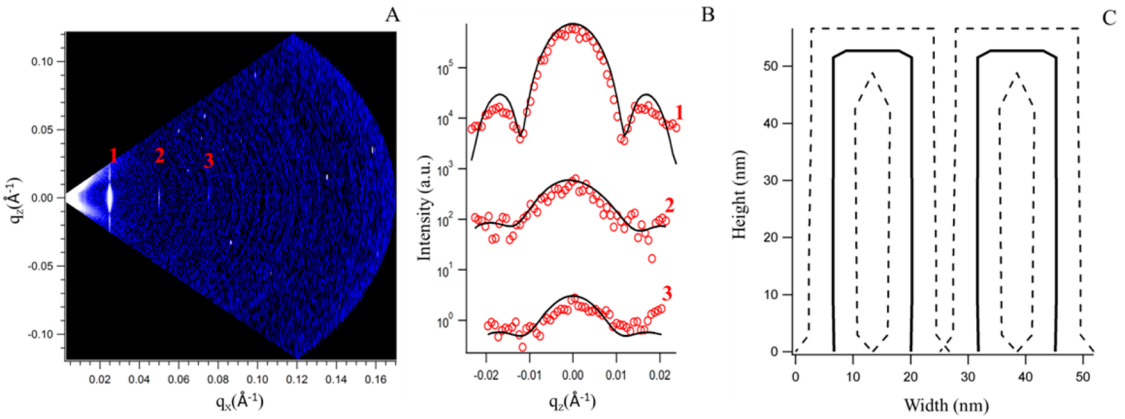

Figure 3. (A) $I(q_x,q_z)$ map obtained from CDSAXS measurements on DSA1 @17 keV, (B) q_z cuts and best fit to the data (○ experimental data, — simulated fit), (C) 3 trapezoid model used to simulate the scattering. Solid lines indicate best model fit to the PMMA lamella; PS lamella are the same thickness and fill the space between the PMMA lamella. Dashed lines outline 95% confidence interval on fit uncertainty. Two unit cells are shown in order to better illustrate the structure.

topological constraints induced by the thicker template. The NRCP brush used in this simulation is thicker than generally used in real applications, but it effectively illustrates the impact the topological aspect of the template can bring to the buried features of the BCP. Figure 2C shows the case where a thickness ratio of 3:7 was used for the chemical pattern, for these simulations a thicker pinning stripe results in a greater effective attraction for the PMMA block. These conditions generate different morphologies for the on-brush lamella compared to the on-substrate lamella. The on-brush lamella have a constant width throughout the depth of the profile, but begin to tilt as the lamella approach the substrate surface. Complete disruption of the lamellar microstructure is observed for the on-substrate lamella, where the morphology appears to be a mixture of parallel and perpendicular lamella. Simulations where the substrate thickness increases further (not shown here) increasingly resemble the parallel lamella morphology, although all of the results retain some perpendicular character on the NRCP brush. Nealey and co-workers have observed similar results, where their simulations showed surface profiles having effective registration accompanied by complete disruption of the buried morphologies.[12] While top down characterization methods typically used to evaluate DSA BCP films would observe identical morphologies for all three of these results, the simulated res-CDSAXS reciprocal space maps which accompany the simulation results demonstrate the potential ability of the method to differentiate between even relatively small changes in the internal structure. The simulated scattering profiles demonstrate changes in both the fringe amplitude and period throughout the pattern, demonstrating the potential sensitivity of res-CDSAXS.

A series of four samples was produced where the width of the chemical template was systematically varied, these are labeled DSA1−DSA4 (where DSA1 had the smallest template width and DSA4 the largest). The $I(q_x,q_z)$ map for DSA1 obtained from conventional CDSAXS measurements at 17 keV is shown in Figure 3A. Three primary scattering peaks can be observed, where only the first order peak shows significant deviation from the background scattering. The shape of the curves can be seen more clearly in the q_z cuts shown in Figure 3B. A model consisting of a single repeating unit cell of PS and PMMA lamella was used to simulate the scattering, and the model fit to the scattering is shown in Figure 3C, where the solid lines represent the best fit to the PMMA lamella and the dashed lines show the 95% confidence intervals in the dimensions of the PMMA domains as determined by the MCMC algorithm. The combination of only three peaks along with a narrow range of data in the q_z direction leads to a highly ambiguous fit to the scattering, as shown in Figure 3C where a wide variety of structures can be generated which satisfactorily fit the data. Aside from the sample pitch, which can be approximated based on the peak spacing along the q_x axis, relatively little definitive information can be obtained on the internal film structure. The weak scattering results from insufficient contrast between the PS and PMMA components of the BCP, which is on the order of 10% at 17 keV. Resonant soft X-rays near the carbon absorption edge will be used to improve the contrast.

The res-CDSAXS $I(q_x,q_z)$ map for DSA1 is shown in Figure 4 for an energy of 282 eV, which is below the absorption edge for carbon. In contrast to the hard X-ray measurement five primary peaks can be observed, all of which have a much wider range in the q_z direction than seen in the conventional CDSAXS data. Scattering peaks are observed at periodic q_x intervals corresponding to two different length scales within the sample. The primary scattering peaks labeled with red numerals have an average $\langle \Delta q_x \rangle$ = 0.0251 Å^{-1}, corresponding to a pitch of 25.1 ± 0.2 nm,

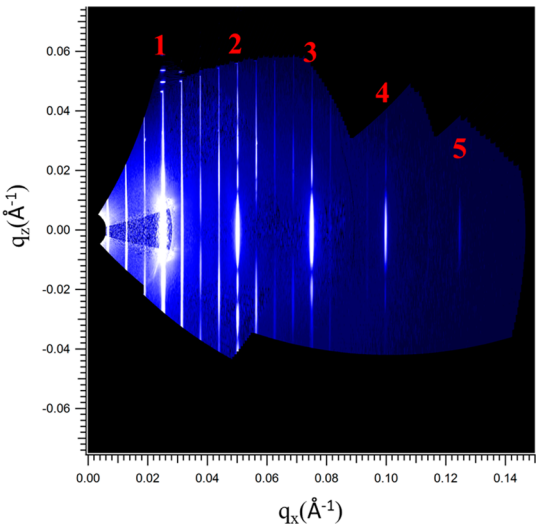

Figure 4. $I(q_x,q_z)$ map obtained from res-CDSAXS measurements of DSA1 at 282 eV, reconstructed from over 400 individual images. Red numerals indicate primary scattering peaks corresponding to the BCP lamellar pitch; unlabeled peaks correspond to the superlattice pitch. The cone shaped scattering observed at low q_x is a reconstruction artifact.

which is the pitch of the native PS-*b*-PMMA ($P = 2\pi/\langle\Delta q_x\rangle$). The satellite peaks are observed at a quarter of that distance ($\langle\Delta q_x\rangle = 0.00624$ Å^{-1}), resulting in a pitch of 100.6 ± 0.1 nm, which arises from a superlattice structure originating from the chemical template. The scattering peaks at the superlattice positions arise from a combination of scattering from the buried chemical template and satellite peaks from the lamella BCP resulting from periodic fluctuations in the lamella pitch caused by the DSA process. For all peak orders the curves are nominally symmetric with the center position of the curve falling along $q_z = 0$. This indicates the lamella are aligned normal to the substrate and lack any net tilt, which would result in the curve center being offset from $q_z = 0$.

In order to demonstrate that the scattering obtained at 282 eV contained sufficient information to uniquely differentiate between the lamellar shapes on and off the NRCP brush we considered two models. The first utilized a single BCP lamellar profile and assumed that the scattering from the chemical template was insufficiently intense to impact the shape of the primary peaks (this assumption was necessary as inclusion of the chemical template would have forced the use of different lamellar profiles on the template). The second included the chemical template and defined the lamellar shape using two different profiles depending on whether the lamella were located on the NRCP brush or the substrate. The biggest challenge in fitting inverse data is the lack of a unique solution, without prior knowledge obtained from real space methods to narrow the parameter space it is possible for simulated scattering from multiple candidate structures to satisfactorily match the experimental profile. If the simple grating model proved to be as effective as the more complex model in fitting the scattering data this would demonstrate there was insufficient information in the scattering map to resolve the minor details present in the sample.

The best fit to the scattering data obtained from the single profile model is shown in Figure 5A. It can be seen that the simulated scattering mirrors the general shape of the experimental scattering, but is unable to satisfactorily recreate several details of the curves. Significant deviations in shape are observed for the third and fifth order peaks, while the simulated scattering at the second and fourth order peaks qualitatively follows the experimental data but is unable to sufficiently match the intensity. As a general rule for reciprocal space methods, smaller features contribute greatest to higher peak orders, meaning that the lowest order peaks correspond to the general outline of the structure while the higher order peaks correspond to smaller structural features. This suggests that the single grating model captures the approximate shape of the internal film structure, but lacks the complexity necessary to reconstruct the finer details of the scattering.

The structure of DSA1, determined using a model which includes scattering from the chemical template and differentiates between the on-brush and on-substrate lamella, is shown in Figure 5B. The multiple profile model clearly improves the match of the simulated and experimental scattering, particularly for the second, third and fifth order peaks (≈ 43% reduction in χ^2). The chemical template is outlined by a solid purple line, and was found to be 54.4 ± 0.8 nm wide and 8.8 ± 0.7 nm thick. The PMMA lamella are outlined by the solid black lines with the 95% confidence intervals for the fits indicated by dotted lines. Each of the lamellar fits represent the average profile along that line, and as a result samples that have a distribution of nonperiodic features along the lines can result in average profiles which may appear unphysical. The presence of heterogeneous features along a given line will manifest in the model in the form of a larger *DW* factor, indicating a wider interfacial width, and will be discussed in detail later in the document. The on-substrate PMMA lamella in DSA1 show considerable widening at their base, this likely results from the much higher affinity of the PMMA block for the underlying antireflective coating (ARC) compared to the PS block. Above the substrate the PMMA lamella narrow quickly, followed by mild width oscillations until the upper half of the profile which gradually widens as the surface is approached. Within two nanometers of the surface the lamella quickly narrow to a width of 2.7 ± 1.4 nm at the surface; this surface enrichment of PS results from the lower surface energy of PS compared to PMMA. By comparison the PMMA lamella on the neutral brush exhibit a less complex profile. Slight necking occurs above the brush-polymer interface followed by mild

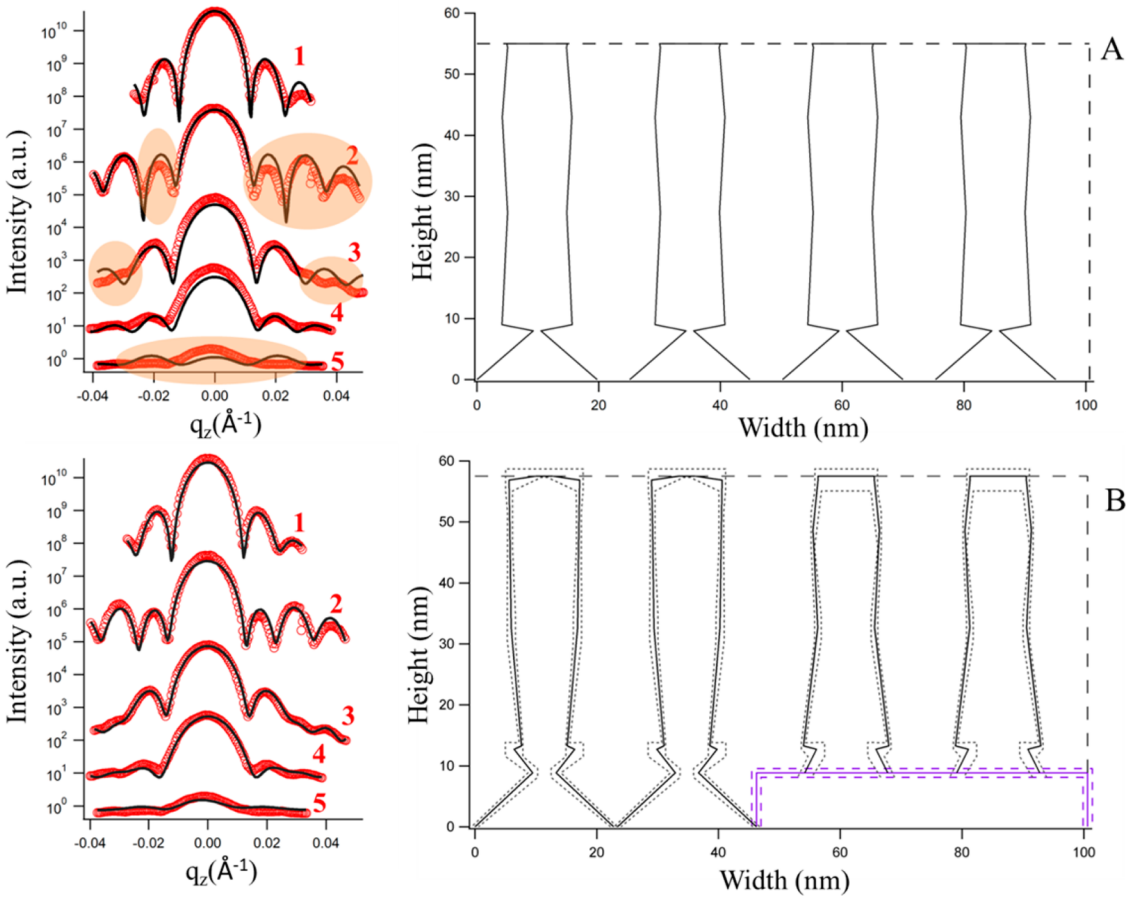

Figure 5. q_z cuts and model fits to the data from the $I(q_x,q_z)$ map of DSA1 (282 eV) (○ experimental data, — simulated fit). (A) Model fits from a single lamella structure, showing four repeat units encompassing the template defined superlattice pitch. Solid black lines outline the PMMA lamella; PS lamella are bordered by long dashed lines. The simulated scattering from the single grating provides inadequate fit to the experimental data at the 2nd, 3rd and 5th order peaks as shown in the highlighted regions. (B) Model fits using a multiple lamellar profiles. Solid black lines indicate the outline of the PMMA lamella; PS lamella are bordered by the long dashes. 95% confidence intervals for PMMA lamella are shown by the dotted lines, and the purple solid and dashed lines represent best fits and 95% confidence intervals for the NRCP brush, respectively.

width oscillations along the profile. Similarly to the on-substrate PMMA lamella the profile narrows sharply as the surface is approached. The stresses induced by the interfacial energy of the brush-lamella interactions are by design much lower than those induced at the substrate BCP interface. This difference likely accounts for the more significant deviation from the native lamellar shape observed for the on-substrate PMMA lamella. The internal structure of this film closely resembles the morphology predicted by the MC calculations, including the narrowing of the on-substrate lamella and the simpler behavior seen for the on-brush lamella. The average PS volume fraction in the film was calculated to be 55%, while the volume fraction at the surface (defined as the volume fraction within 3 nm of the surface) was determined to be 70% PS. This agrees with the composition determined independently by surface sensitive NEXAFS measurements, which are shown in the Supporting Information.

The topographical constraints imposed by the polymer brush have the potential to disrupt the native pitch and shape of the BCP, inducing offsets which are likely to transfer through the etch process. When deposited on an unpatterned neutral surface the native PS-*b*-PMMA pitch is 25.1 nm. The pitches observed in this sample, as determined by the center−center distance between the PMMA lamella, can be seen to deviate significantly from the equilibrium values. The spacing between the on-brush lamella comes the closest to matching the native spacing at 25.0 ± 0.2 nm. The spacing between the lamella on the ARC and brush is much larger, at 26.2 ± 0.4 nm, with the center−center distance between the on-substrate lamella being 23.41 ± 0.4 nm. This shows that the stresses on the polymer lamella induced by the chemistry and topography of the template will be mediated within the film both by oscillations in the lamellar profile and by deviations from the equilibrium pitch. It is unclear how these types of stresses will impact the LER/LWR of the BCP, or how these parameters will translate through the etch process. The *DW* factor for this sample was determined to be 1.99 ± 0.03 nm.

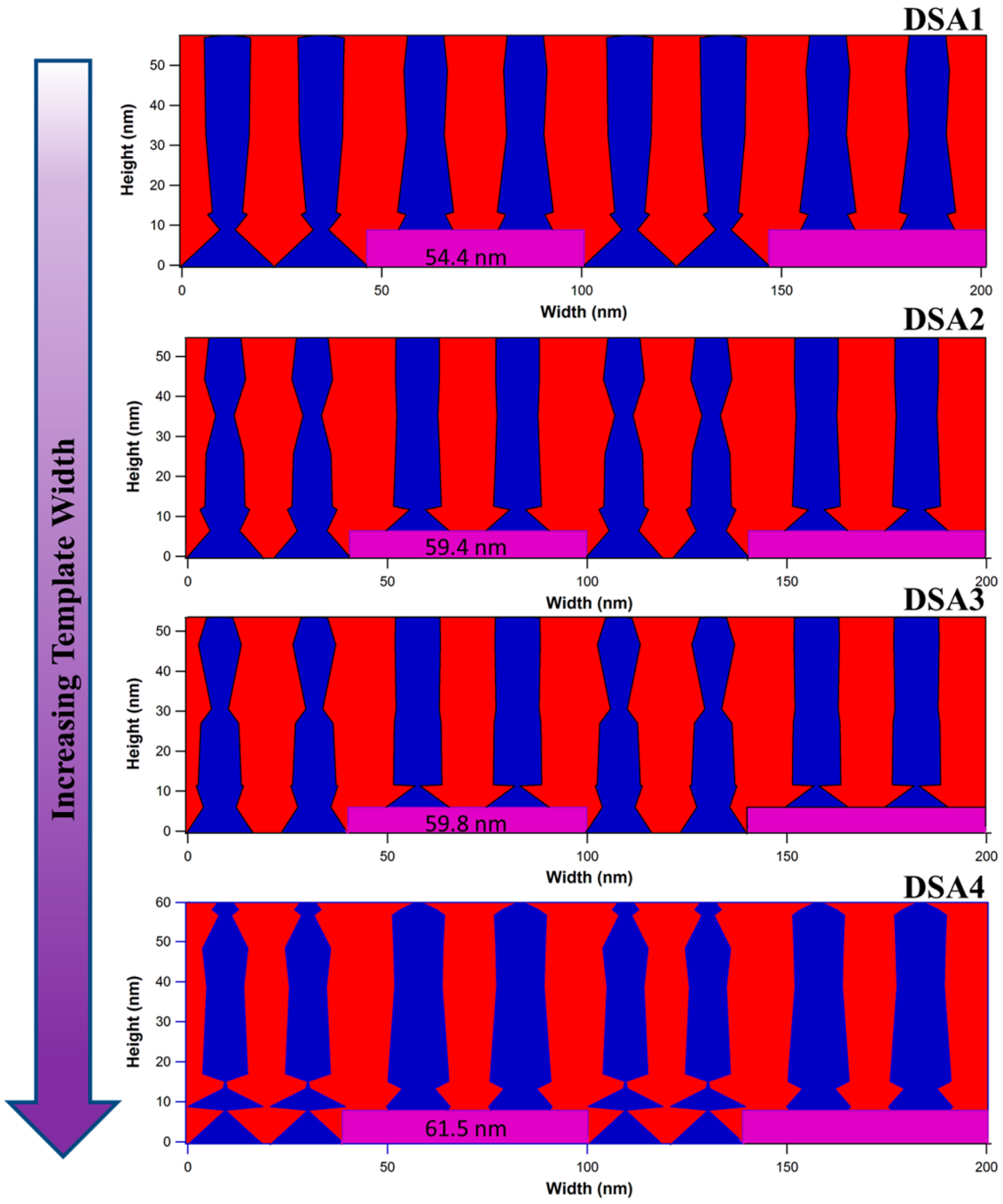

Figure 6. Internal film structures of DSA1−4, in order of increasing template width. Purple areas represent the neutral PS-r-PMMA brush, blue areas PMMA and red PS. Two unit cells of the overall superlattice are shown for each sample in order to provide a better visual representation. Uncertainties on DSA2−4 are shown in the Supporting Information.

The *DW* factor is a measure of the interfacial width between the BCP lamella and contributes to the scattering in the form of an exponential decay factor as seen in eq 3. The *DW* factor is proportional to the interfacial width between the lamella, which in these samples is combination of the component distribution through the interface convolved with the LER and LWR. Fluctuations in the morphology along the lines and variations in the 3D structure will also increase the *DW* factor. It is unlikely that the interfacial widths will be identical for both the on-substrate and on-brush lamella given the variation in stresses present in the sample. It is unclear at this time if it is possible to deconvolute contributions to the *DW* factor from the different lamella into their component parts, and this result should be taken to represent the average behavior of the component structures.

Figure 6 represents the structures determined for DSA 1−4 as a function of template width. The template for DSA 2 was found to be wider than DSA1 at 59.4 ± 0.9 nm. The 5 nm change in template width results in only minor differences to the on-brush lamella, but a significant change to the on-substrate lamella.

The on-brush lamella show slightly more severe necking at the base, but otherwise exhibit only small variations in width (<1.5 nm) before reaching the surface. The on-substrate lamella behave similarly to DSA 1 near the base, with PMMA lamella widening at the substrate followed by minor necking. Further up the profile, between 30 and 40 nm in height, the profile width narrows to 4.6 ± 1.2 nm. There is no immediately apparent driving force for narrowing along the lamellar profile at that depth in the film. The MC simulations predict the necking observed near the base of the lamella, but none of the simulation results in this document or the broader literature predict the type of narrowing that is observed between heights of 30 and 40 nm. This raises the possibility that the sample contains a mixture of complete and broken lamella, such as those seen in the MC simulations (Figure 2C) and the simulations reported by de Liu *et al.*[12] res-CDSAXS is an ensemble average technique and the reciprocal space map contains the scattering from the average structure in the sample over the coherence length of the radiation in the incident beam. The combination of broken and complete lamella, or broken lamella with a distribution of breakage locations, when averaged could present the type of feature seen in DSA2. DSA3 has a very similar morphology to DSA2 (the scattering patterns are nearly identical), the primary difference being in the location of the profile narrowing, which occurs just above a height of 30 nm. The *DW* factors for DSA2 and DSA3 were 2.43 ± 0.03 nm and 2.44 ± 0.04 nm, respectively. The increase in *DW* compared to DSA1 supports the hypothesis that there is a distribution of structures in the sample as the combination of complete and broken lamella will result in a wider average interface between the PMMA and PS blocks. DSA4 has the widest template of any of the samples, at 61.5 ± 0.8 nm, and clearly shows the presence of broken lamella above the substrate. The average profile shows the PMMA lamella wetting the substrate and then narrowing to under 1 nm then stretching to 18.8 ± 0.9 nm and collapsing down to 0.2 ± 0.2 nm. Between 18 and 50 nm in height the structure shows continuous, unbroken lamella, before another unusual behavior is observed near the surface where the profile narrows and then re-expands before reaching the PS enriched surface. Again, the driving force for the formation of this feature is not immediately apparent, suggesting that it originates from the averaging of a variety of disrupted lamellar morphologies. DSA2−4 are excellent representations of the type of buried structure that cannot be observed through top-down evaluation methods.

3σ LER and LWR values for DSA2−4 were calculated from an edge analysis of top-down SEM images on etched samples and were found to be 2.2, 2.2 and 2.1 nm for LER and 2.4, 2.3 and 2.3 nm for LWR for samples DSA2−4, respectively. The equivalent 3σ for the *DW* factor are 7.29, 7.32 and 8.55 nm, significantly larger than the values determined from SEM. The *DW* factor includes contributions from the interfaces throughout the entire thickness of the film, whereas the SEM of etched samples is biased toward the roughness at the top. The *DW* factor is also sensitive to compositional heterogeneity between the BCP components (interfacial mixing), and this likely the source of some of the difference in the values. Finally, if an appreciable volume fraction of the PS lines are floating on layers of PMMA, this will increase the *DW* factor, but not be observed by the SEM analysis. The connection between the *DW* factor and LER is the subject of ongoing research.

CONCLUSIONS

The BCP DSA process depends on a complex set of stresses induced by the chemical template to enable long-range orientation of a BCP. Developing a deeper understanding of the physics involved with the assembly process will be the critical component in the continued development of the technology. We have demonstrated that res-CDSAXS is capable of interrogating the buried features within a BCP, which were previously observed only through simulations. The comparison of DSA1−4 provides an excellent demonstration of the variety of morphologies that can arise from small fluctuations in key process parameters, which may be unobservable through other methods. This measurement will enable the connection of simulation results to relevant process parameters, improving our understanding of the assembly mechanism and potentially yielding process improvements that will accelerate the implementation of BCP DSA.

MATERIALS AND METHODS

Sample Preparation and Film Delamination. DSA BCP's were prepared according to previously reported procedures.[11,29,49] Briefly, a resist was patterned at a 100 nm pitch using 193 nm water immersion lithography and this pattern was used to template the neutral random copolymer brush (NRCP). The resist was removed *via* a liftoff procedure and the PS-*b*-PMMA was spin coated on top of the NRCP pattern followed by a brief anneal at 240 °C. PS-*b*-PMMA (M_n = 22 kg/mol-*b*-22 kg/mol, PDI = 1.09) was purchased from Polymer Source. The DSA BCP layer was delaminated from the silicon substrate and transferred to a silicon nitride window *via* the following method. A thin layer of amorphous carbon was evaporated onto the BCP film followed by a coating of poly(acrylic acid) (PAA) in H_2O (25% by mass). The PAA coated sample was then placed in a 55 °C oven for 6 h in order to dry. The DSA film and underlying layers then adhere to the PAA layer and can be delaminated from the underlying substrate. The detached film is placed into a sample dish with deionized water (PAA side down) until the PAA layer dissolves. The free-standing film can then be float transferred to a silicon nitride window (Norcada NX5150C, 1.5 mm by 1.5 mm wide window with a thickness of 100 nm).

CD-SAXS Experimental and Analysis Procedures. Soft X-ray measurements were conducted at the 11.0.1.2 beamline at the Advanced Light Source (ALS) at Lawrence Berkeley National Laboratory.[50] The sample chamber was maintained under high vacuum (10^{-5} Pa) at 282 eV, all samples were transferred to SiN windows using the previously described procedure. A pre-edge energy of 282 eV was selected to give enhanced sensitivity while minimizing the absorption and potential sample damage. The beam was circular and had a spot size of approximately 300 μm. Collection time varied from 0.1 to 60 s depending on the sample and detector angles to maximize signal-to-noise. Hard X-ray measurements were conducted at the 5-ID D beamline at the Advanced Photon Source (APS) at Argonne National Laboratory. The incident energy was 17 keV and each sample angle was measured for 60 s. For both beamlines a charge coupled device (CCD) detector was used, and the scattering vector was calibrated with a grating sample of known pitch. The DSA sample was placed on a rotation stage such that the line gratings were parallel to the axis of rotation, which was aligned to coincide with the beam center. Scattering from the three-dimensional sample (with the scattering vector **q** defined as q_x, q_y, q_z as shown in Figure 1a) is then projected onto the 2-D detector (with **q** vectors of q_{xz}, q_y). q_{xz} is transformed to q_x and q_z using eqs 1a and 1b. The individual images from all angles are then reconstructed into a 2D reciprocal space map.

$$q_x = q_{xz} \times \sin\left(\varphi - \frac{2\theta}{2}\right) \quad (1a)$$

$$q_z = q_{xz} \times \cos\left(\varphi - \frac{2\theta}{2}\right) \quad (1b)$$

The simulated scattering intensity from the proposed model structure is calculated from eqs 2 and 3 where $\rho(\mathbf{r})$ is the shape function including contrast, P is the pitch, * represents a convolution and DW is the Debye–Waller factor, which accounts for interfacial roughness.

$$I_o(\mathbf{q}) = \left| \int_A \rho(\mathbf{r}) * \sum_n \delta(x - n \times P) e^{-i\mathbf{qr}}\, d\mathbf{r} \right|^2 \quad (2)$$

$$I(\mathbf{q}) = I_o(\mathbf{q}) \times e^{-\mathbf{q}^2 DW^2} \quad (3)$$

The model was fit to linecuts from the experimental data in both the q_x and q_z directions. Once the best fit was obtained the uncertainty in the fit was determined using a Monte Carlo Markov Chain (MCMC) algorithm with a Metropolis–Hastings sampler as the acceptance criteria.[51,52] The best known fit to the model is used as the initial condition, candidate models are then generated through random perturbations to the initial model parameters, with the step size for the changes randomly generated each iteration. Candidate models that improve on the fit from the prior step in the chain are always accepted, while the acceptance criteria for candidates that have worse fits is as follows. An acceptance probability (α) is generated based on the relative fit quality of the candidate model compared to the current model. The acceptance variable $y \in [0,1]$ is generated, and if $y < \alpha$, the candidate model is accepted.[52] The model population developed from the MCMC is then resampled every 200 steps to remove correlations between points. A sufficiently large model population was generated to ensure that the sampled distribution had reached equilibrium. Uncertainties reported are 95% confidence intervals as determined from the resampled population.

Single Chain in Mean Field Monte Carlo Simulations. Single chain in mean field Monte Carlo (MC) simulations[53] were used to generate representative three-dimensional structures of the BCP films atop the patterned substrate. The lamella-forming polymer was represented by a compressible 40-bead chain with equal fractions of PS and PMMA beads and with Doi–Edwards bonds of equilibrium length 2.9 nm, $\chi N = 16\ k_BT$ and $\kappa = 25\ k_BT$, yielding a bulk lamellar pitch of 28 nm. Simulations were carried out on a lattice with 1 nm spacing at a bead number density of 20 beads/nm^3. In the simulations, the substrate was patterned with a pinning stripe of 42 nm (1.5 L_0) at a pitch of 112 nm (4 L_0). The width of the simulation cell was fixed at 28 nm but the height (film thickness) was varied from 14 to 80 nm. Additional simulations were carried out for bulk pitches of 28 and 30 nm, for pinning stripes of 0.5 L_0 and 1.5 L_0, and for both 3× and 4× multiplication, but are not reported here. Static densities of half the bulk density of the polymer were used to represent the substrate patterning, with the pinning regions having a 5.0 k_BT repulsion for PS and neutral regions having no repulsion for either bead type. The height of these static densities representing brush regions defining the pinning stripe and neutral brush were varied systematically and independently from 1 to 14 nm. The top of the film was modeled as a neutral interface for both PS and PMMA. Simulations were seeded with initial configurations where uniform full-thickness lamellae were assembled either in or out of register (misaligned by 0.5 L_0) with the pinning stripe and then allowed to evolve for 5000 Monte Carlo sweeps, where each sweep involved on average one Monte Carlo move per monomer. The final bead distributions were visualized using OpenDX.[54]

Conflict of Interest: The authors declare no competing financial interest.

Acknowledgment. Portions of this work were performed at the DuPont-Northwestern-Dow Collaborative Access Team (DND-CAT) located at Sector 5 of the Advanced Photon Source (APS). DND-CAT is supported by E.I. DuPont de Nemours & Co., The Dow Chemical Company and Northwestern University. Use of the APS, an Office of Science User Facility operated for the U.S. Department of Energy (DOE) Office of Science by Argonne National Laboratory, was supported by the U.S. DOE under Contract No. DE-AC02-06CH11357. The Advanced Light Source is supported by the Director, Office of Science, Office of Basic Energy Sciences, of the U.S. Department of Energy under Contract No. DE-AC02-05CH11231. We thank Steven Weigand and Denis Keane for assistance at sector 5-ID-D and Anthony Young and Cheng Wang for assistance at BL 11.0.1.2. Authors JWP, MT and JC acknowledge the financial support of the IBM Corporation and experiment support from Christopher Bencher and Applied Materials. Certain commercial equipment, instruments, or materials are identified in this paper in order to specify the experimental procedure adequately. Such identification is not intended to imply recommendation or endorsement by the National Institute of Standards and Technology, nor is it intended to imply that the materials or equipment identified are necessarily the best available for the purpose.

Supporting Information Available: Figures S1–S4. This material is available free of charge *via* the Internet at http://pubs.acs.org.

REFERENCES AND NOTES

1. *The International Technology Roadmap for Semiconductors*, 2013; http://www.itrs.net/.
2. Moors, R.; Banine, V.; Swinkels, G.; Wortel, F. Extreme-Ultraviolet Source Specifications: Tradeoffs and Requirements. *J. Micro/Nanolithogr., MEMS, MOEMS* **2012**, *11*, 021102.
3. Ofir, Y.; Moran, I. W.; Subramani, C.; Carter, K. R.; Rotello, V. M. Nanoimprint Lithography for Functional Three-Dimensional Patterns. *Adv. Mater.* **2010**, *22*, 3608–3614.
4. Chang, T. H. P.; Mankos, M.; Lee, K. Y.; Muray, L. P. Multiple Electron-Beam Lithography. *Microelectron. Eng.* **2001**, *57*, 117–135.
5. Saavedra, H. M.; Mullen, T. J.; Zhang, P.; Dewey, D. C.; Claridge, S. A.; Weiss, P. S. Hybrid Strategies in Nanolithography. *Rep. Prog. Phys.* **2010**, *73*, 036501.
6. Stoykovich, M. P.; Müller, M.; Kim, S. O.; Solak, H. H.; Edwards, E. W.; de Pablo, J. J.; Nealey, P. F. Directed Assembly of Block Copolymer Blends into Nonregular Device-Oriented Structures. *Science* **2005**, *308*, 1442–1446.
7. Edwards, E. W.; Stoykovich, M. P.; Müller, M.; Solak, H. H.; de Pablo, J. J.; Nealey, P. F. Mechanism and Kinetics of Ordering in Diblock Copolymer Thin Films on Chemically Nanopatterned Substrates. *J. Polym. Sci., Part B: Polym. Phys.* **2005**, *43*, 3444–3459.

8. Kim, S. O.; Kim, B. H.; Kim, K.; Koo, C. M.; Stoykovich, M. P.; Nealey, P. F.; Solak, H. H. Defect Structure in Thin Films of a Lamellar Block Copolymer Self-Assembled on Neutral Homogeneous and Chemically Nanopatterned Surfaces. *Macromolecules* **2006**, *39*, 5466–5470.
9. Ruiz, R.; Kang, H.; Detcheverry, F. A.; Dobisz, E.; Kercher, D. S.; Albrecht, T. R.; de Pablo, J. J.; Nealey, P. F. Density Multiplication and Improved Lithography by Directed Block Copolymer Assembly. *Science* **2008**, *321*, 936–939.
10. Bates, F. S.; Fredrickson, G. H. Block Copolymer Thermodynamics: Theory and Experiment. *Annu. Rev. Phys. Chem.* **1990**, *41*, 525–557.
11. Bencher, C.; Yi, H.; Zhou, J.; Cai, M.; Smith, J.; Miao, L.; Montal, O.; Blitshtein, S.; Lavi, A.; Dotan, K.; *et al.* Directed Self-Assembly Defectivity Assessment. Part II. *Proc. SPIE* **2012**, 83230N–83230N-10.
12. Liu, C.-C.; Ramírez-Hernández, A.; Han, E.; Craig, G. S. W.; Tada, Y.; Yoshida, H.; Kang, H.; Ji, S.; Gopalan, P.; de Pablo, J. J.; *et al.* Chemical Patterns for Directed Self-Assembly of Lamellae-Forming Block Copolymers with Density Multiplication of Features. *Macromolecules* **2013**, *46*, 1415–1424.
13. Ji, S.; Nagpal, U.; Liu, G.; Delcambre, S. P.; Müller, M.; de Pablo, J. J.; Nealey, P. F. Directed Assembly of Non-Equilibrium ABA Triblock Copolymer Morphologies on Nanopatterned Substrates. *ACS Nano* **2012**, *6*, 5440–5448.
14. Detcheverry, F. A.; Liu, G.; Nealey, P. F.; de Pablo, J. J. Interpolation in the Directed Assembly of Block Copolymers on Nanopatterned Substrates: Simulation and Experiments. *Macromolecules* **2010**, *43*, 3446–3454.
15. Stoykovich, M. P.; Daoulas, K. C.; Müller, M.; Kang, H.; de Pablo, J. J.; Nealey, P. F. Remediation of Line Edge Roughness in Chemical Nanopatterns by the Directed Assembly of Overlying Block Copolymer Films. *Macromolecules* **2010**, *43*, 2334–2342.
16. Takahashi, H.; Laachi, N.; Delaney, K. T.; Hur, S.-M.; Weinheimer, C. J.; Shykind, D.; Fredrickson, G. H. Defectivity in Laterally Confined Lamella-Forming Diblock Copolymers: Thermodynamic and Kinetic Aspects. *Macromolecules* **2012**, *45*, 6253–6265.
17. Mishra, V.; Fredrickson, G. H.; Kramer, E. J. Effect of Film Thickness and Domain Spacing on Defect Densities in Directed Self-Assembly of Cylindrical Morphology Block Copolymers. *ACS Nano* **2012**, *6*, 2629–2641.
18. Bosse, A. W.; Sides, S. W.; Katsov, K.; García-Cervera, C. J.; Fredrickson, G. H. Defects and Their Removal in Block Copolymer Thin Film Simulations. *J. Polym. Sci., Part B: Polym. Phys.* **2006**, *44*, 2495–2511.
19. Bosse, A. W. Modeling the Power Spectrum of Thermal Line Edge Roughness in a Lamellar Diblock Copolymer Mesophase. *J. Vac. Sci. Technol., B: Microelectron. Nanometer Struct.* **2011**, *29*, 06F202.
20. Perera, G. M.; Wang, C.; Doxastakis, M.; Kline, R. J.; Wu, W.; Bosse, A. W.; Stein, G. E. Directed Self-Assembly of Lamellar Copolymers: Effects of Interfacial Interactions on Domain Shape. *ACS Macro Lett.* **2012**, *1*, 1244–1248.
21. Bosse, A. W.; Lin, E. K.; Jones, R. L.; Karim, A. Interfacial Fluctuations in an Ideal Block Copolymer Resist. *Soft Matter* **2009**, *5*, 4266.
22. Patrone, P. N.; Gallatin, G. M. Modeling Line Edge Roughness in Templated, Lamellar Block Copolymer Systems. *Macromolecules* **2012**, *45*, 9507–9516.
23. Jones, R. L.; Soles, C. L.; Lin, E. K.; Hu, W.; Reano, R. M.; Pang, S. W.; Weigand, S. J.; Keane, D. T.; Quintana, J. P. Pattern Fidelity in Nanoimprinted Films Using Critical Dimension Small Angle X-Ray Scattering. *J. Microlithogr., Microfabr., Microsyst.* **2006**, *5*, 013001.
24. Wang, C.; Jones, R. L.; Lin, E. K.; Wu, W.-L.; Rice, B. J.; Choi, K.-W.; Thompson, G.; Weigand, S. J.; Keane, D. T. Characterization of Correlated Line Edge Roughness of Nanoscale Line Gratings Using Small Angle X-Ray Scattering. *J. Appl. Phys.* **2007**, *102*, 024901.
25. Wang, C.; Jones, R. L.; Lin, E. K.; Wu, W.-L.; Leu, J. Small Angle X-Ray Scattering Measurements of Lithographic Patterns with Sidewall Roughness from Vertical Standing Waves. *Appl. Phys. Lett.* **2007**, *90*, 193122.
26. Stein, G. E.; Liddle, J. A.; Aquila, A. L.; Gullikson, E. M. Measuring the Structure of Epitaxially Assembled Block Copolymer Domains with Soft X-Ray Diffraction. *Macromolecules* **2010**, *43*, 433–441.
27. Yang, X. M.; Peters, R. D.; Nealey, P. F.; Solak, H. H.; Cerrina, F. Guided Self-Assembly of Symmetric Diblock Copolymer Films on Chemically Nanopatterned Substrates. *Macromolecules* **2000**, *33*, 9575–9582.
28. Liu, C.-C.; Han, E.; Onses, M. S.; Thode, C. J.; Ji, S.; Gopalan, P.; Nealey, P. F. Fabrication of Lithographically Defined Chemically Patterned Polymer Brushes and Mats. *Macromolecules* **2011**, *44*, 1876–1885.
29. Cheng, J. Y.; Sanders, D. P.; Truong, H. D.; Harrer, S.; Friz, A.; Holmes, S.; Colburn, M.; Hinsberg, W. D. Simple and Versatile Methods To Integrate Directed Self-Assembly with Optical Lithography Using a Polarity-Switched Photoresist. *ACS Nano* **2010**, *4*, 4815–4823.
30. Edwards, E. W.; Montague, M. F.; Solak, H. H.; Hawker, C. J.; Nealey, P. F. Precise Control over Molecular Dimensions of Block-Copolymer Domains Using the Interfacial Energy of Chemically Nanopatterned Substrates. *Adv. Mater.* **2004**, *16*, 1315–1319.
31. Bates, C. M.; Seshimo, T.; Maher, M. J.; Durand, W. J.; Cushen, J. D.; Dean, L. M.; Blachut, G.; Ellison, C. J.; Willson, C. G. Polarity-Switching Top Coats Enable Orientation of Sub-10-Nm Block Copolymer Domains. *Science* **2012**, *338*, 775–779.
32. Chang, J.-B.; Son, J. G.; Hannon, A. F.; Alexander-Katz, A.; Ross, C. A.; Berggren, K. K. Aligned Sub-10-Nm Block Copolymer Patterns Templated by Post Arrays. *ACS Nano* **2012**, *6*, 2071–2077.
33. Cheng, J. Y.; Mayes, A. M.; Ross, C. A. Nanostructure Engineering by Templated Self-Assembly of Block Copolymers. *Nat. Mater.* **2004**, *3*, 823–828.
34. Cushen, J. D.; Otsuka, I.; Bates, C. M.; Halila, S.; Fort, S.; Rochas, C.; Easley, J. A.; Rausch, E. L.; Thio, A.; Borsali, R.; *et al.* Oligosaccharide/Silicon-Containing Block Copolymers with 5 nm Features for Lithographic Applications. *ACS Nano* **2012**, *6*, 3424–3433.
35. Liu, C.-C.; Thode, C. J.; Rincon Delgadillo, P. A.; Craig, G. S. W.; Nealey, P. F.; Gronheid, R. Towards an All-Track 300 Mm Process for Directed Self-Assembly. *J. Vac. Sci. Technol., B: Microelectron. Nanometer Struct.* **2011**, *29*, 06F203.
36. Araki, T.; Ade, H.; Stubbs, J. M.; Sundberg, D. C.; Mitchell, G. E.; Kortright, J. B.; Kilcoyne, A. L. D. Resonant Soft X-Ray Scattering from Structured Polymer Nanoparticles. *Appl. Phys. Lett.* **2006**, *89*, 124106.
37. Vu, T.; Mahadevapuram, N.; Perera, G. M.; Stein, G. E. Controlling Domain Orientations in Thin Films of AB and ABA Block Copolymers. *Macromolecules* **2011**, *44*, 6121–6127.
38. Busch, P.; Rauscher, M.; Smilgies, D.-M.; Posselt, D.; Papadakis, C. M. Grazing-Incidence Small-Angle X-Ray Scattering from Thin Polymer Films with Lamellar Structures—the Scattering Cross Section in the Distorted-Wave Born Approximation. *J. Appl. Crystallogr.* **2006**, *39*, 433–442.
39. Hu, T.; Jones, R. L.; Wu, W.; Lin, E. K.; Lin, Q.; Keane, D.; Weigand, S.; Quintana, J. Small Angle X-Ray Scattering Metrology for Sidewall Angle and Cross Section of Nanometer Scale Line Gratings. *J. Appl. Phys.* **2004**, *96*, 1983.
40. Sunday, D. F.; Hammond, M. R.; Wang, C.; Wu, W.; Kline, R. J.; Stein, G. E. Three-Dimensional X-Ray Metrology for Block Copolymer Lithography Line-Space Patterns. *J. Micro/Nanolithogr., MEMS, MOEMS* **2013**, *12*, 031103.
41. Wang, C.; Choi, K.-W.; Chen, Y.-C.; Price, J.; Ho, D. L.; Jones, R. L.; Soles, C.; Lin, E. K.; Wu, W.-L.; Bunday, B. D.; Allgair, J. A.; Raymond, C. J. Nonplanar High-K Dielectric Thickness Measurements Using CD-SAXS. *Proc. SPIE* **2009**, *7272*, 72722M–72722M-8.
42. Harton, S. E.; Stevie, F. A.; Zhu, Z.; Ade, H. Changes in Thermodynamic Interactions at Highly Immiscible Polymer/Polymer Interfaces due to Deuterium Labeling. *J. Phys. Chem. B* **2006**, *110*, 10602–10605.
43. Ade, H.; Wang, C.; Garcia, A.; Yan, H.; Sohn, K. E.; Hexemer, A.; Bazan, G. C.; Nguyen, T.-Q.; Kramer, E. J. Characterization of Multicomponent Polymer Trilayers with Resonant Soft

X-Ray Reflectivity. *J. Polym. Sci., Part B: Polym. Phys.* **2009**, *47*, 1291–1299.
44. Yan, H.; Wang, C.; Garcia, A.; Swaraj, S.; Gu, Z.; McNeill, C. R.; Schuettfort, T.; Sohn, K. E.; Kramer, E. J.; Bazan, G. C.; *et al.* Interfaces in Organic Devices Studied with Resonant Soft X-Ray Reflectivity. *J. Appl. Phys.* **2011**, *110*, 102220.
45. Wang, C.; Araki, T.; Watts, B.; Harton, S.; Koga, T.; Basu, S.; Ade, H. Resonant Soft X-Ray Reflectivity of Organic Thin Films. *J. Vac. Sci. Technol., A* **2007**, *25*, 575.
46. Wang, C.; Lee, D. H.; Hexemer, A.; Kim, M. I.; Zhao, W.; Hasegawa, H.; Ade, H.; Russell, T. P. Defining the Nanostructured Morphology of Triblock Copolymers Using Resonant Soft X-Ray Scattering. *Nano Lett.* **2011**, *11*, 3906–3911.
47. Kinane, C. J.; Suszka, A. K.; Marrows, C. H.; Hickey, B. J.; Arena, D. A.; Dvorak, J.; Charlton, T. R.; Langridge, S. Soft X-Ray Resonant Magnetic Scattering from an Imprinted Magnetic Domain Pattern. *Appl. Phys. Lett.* **2006**, *89*, 092507.
48. Wilkins, S.; Hatton, P.; Roper, M.; Prabhakaran, D.; Boothroyd, A. Soft X-Ray Resonant Magnetic Diffraction. *Phys. Rev. Lett.* **2003**, 90.
49. Bencher, C.; Smith, J.; Miao, L.; Cai, C.; Chen, Y.; Cheng, J. Y.; Sanders, D. P.; Tjio, M.; Truong, H. D.; Holmes, S.; Herr, D. J. C.; *et al.* Self-Assembly Patterning for Sub-15nm Half-Pitch: A Transition from Lab to Fab. *Proc. SPIE* **2011**, *7970*, 79700F–79700F-9.
50. Gann, E.; Young, A. T.; Collins, B. A.; Yan, H.; Nasiatka, J.; Padmore, H. A.; Ade, H.; Hexemer, A.; Wang, C. Soft X-Ray Scattering Facility at the Advanced Light Source with Real-Time Data Processing and Analysis. *Rev. Sci. Instrum.* **2012**, *83*, 045110.
51. Aster, R. C.; Borchers, B.; Thurber, C. H. *Parameter Estimation and Inverse Problems*, 2nd ed.; Academic Press: Waltham, MA, 2013.
52. Mosegaard, K.; Sambridge, M. Monte Carlo Analysis of Inverse Problems. *Inverse Probl.* **2002**, *18*, R29.
53. Muller, M.; Smith, G. D. Phase Separation in Binary Mixtures Containing Polymers: A Quantitative Comparison of Single-Chain-in-Mean-Field Simulations and Computer Simulations of the Corresponding Multichain Systems. *J. Polym. Sci., Part B: Polym. Phys.* **2005**, *43*, 934–958.
54. *OpenDX*; www.opendx.org.